

Positive Semi-definite Latent Factor Grouping-Boosted Cluster-reasoning Instance Disentangled Learning for WSI Representation

Chentao Li , Graduate Student Member, IEEE, Behzad Bozorgtabar , Yifang Ping , Pan Huang , Member, IEEE and Jing Qin , Senior Member, IEEE

Abstract—Multiple instance learning (MIL) has been widely used for representing whole-slide pathology images. However, spatial, semantic, and decision entanglements among instances limit its representation and interpretability. To address these challenges, we propose a latent factor grouping-boosted cluster-reasoning instance disentangled learning framework for whole-slide image (WSI) interpretable representation in three phases. First, we introduce a novel positive semi-definite latent factor grouping that maps instances into a latent subspace, effectively mitigating spatial entanglement in MIL. To alleviate semantic entanglement, we employ instance probability counterfactual inference and optimization via cluster-reasoning instance disentangling. Finally, we employ a generalized linear weighted decision via instance effect re-weighting to address decision entanglement. Extensive experiments on multicentre datasets demonstrate that our model outperforms all state-of-the-art models. Moreover, it attains pathologist-aligned interpretability through disentangled representations and a transparent decision-making process. Code and models will be available at <https://github.com/Prince-Lee-PathAI/PG-CIDL>.

Index Terms—Pathology, Whole-slide image, Multiple Instance Learning, Representation, Deep Clustering

I. INTRODUCTION

WHOLE slide images (WSIs), the gold standard for pathological classification, play a vital role in clinical tasks such as diagnosis, prognosis, and metastasis prediction [1]. Multiple instance learning (MIL) has emerged as a promising approach for computational gigapixel WSIs analysis. It

is a typical weakly supervised learning framework, where slide-level (bag) labels are available, while abundant instance-level (patch) labels within each slide are few annotated. Existing MIL frameworks suffer from weak interpretability because of entangled instance features from three aspects, *i.e.* spatial entanglement, semantic entanglement and decision entanglement; see Figure 1.

Spatial entanglement arises when spatially adjacent instances exhibit correlated yet distinct pathological factors. It leads the model to confuse their individual contributions due to the absence of explicit spatial constraints. For example, the mixed tumor boundary and inflammatory areas make it difficult to distinguish the pathological border in spatial context. Typically, ABMIL [2] selects top-k patches as positive instances based on attention scores. ACMIL [3] extends this by introducing multi-branch attention and stochastic top-k masking to capture diverse informative instances. Including TransMIL [4], these attention-based MIL framework [2]–[7] generate attention scores that merely reflect the correlation between instances and bag-level predictions. They are incapable of modeling how instances contribute to pathological spatial patterns [8].

Despite spatial disentanglement, the inability to determine the factor group for each instance still hinders the model's interpretability and representation. From the standpoint of genetic biology, tumor regions are more closely linked to pathological manifestations than non-tumor areas [9]. However, conventional MIL models under weak supervision lack explicit semantic guidance, thus fusing tumor and non-tumor into unified latent representation. This semantic entanglement fails the model to distinguish which regions are truly responsible for the diagnostic outcome; see Figure 1. Consequently, the learned instance weights fail to relate with pathological factors, which undermines model interpretability and alignment with pathological priors. To this end, cluster-incorporated MILs have been explored in WSI analysis. Panther [10] is a prototype-based approach with Gaussian mixture model that summarizes WSI patches into a smaller set of morphological prototypes, transporting into refined WSI features. FuzzyMIL [11] decouples morphological patterns in WSIs through a learnable deep fuzzy clustering framework while cDPMIL [12] models the instance-to-bag structure using a cascade of Dirichlet processes based on feature covariance. These

Corresponding author: Pan Huang.

Chentao Li is with the Fu Foundation School of Engineering and Applied Science, Columbia University, New York, NY 10027, USA (e-mail: cl4691@columbia.edu).

Behzad Bozorgtabar is with the Signal Processing Laboratory (LT55), École Polytechnique Fédérale de Lausanne (EPFL), 1015 Lausanne, Switzerland, and also with the Radiology Department, Centre Hospitalier Universitaire Vaudois, 1005 Lausanne, Switzerland (e-mail: behzad.bozorgtabar@epfl.ch).

Yifang Ping is with the Jingfeng Laboratory, Chongqing, China (e-mail: pingyifang@126.com).

Pan Huang is with the Centre for Smart Health, School of Nursing, The Hong Kong Polytechnic University, Hong Kong 999077, SAR China, and also with the Jingfeng Laboratory, Chongqing, China (e-mail: pan-huang@polyu.edu.hk).

Jing Qin is with the Centre for Smart Health, School of Nursing, The Hong Kong Polytechnic University, Hong Kong 999077, SAR China (e-mail: harry.qin@polyu.edu.hk).

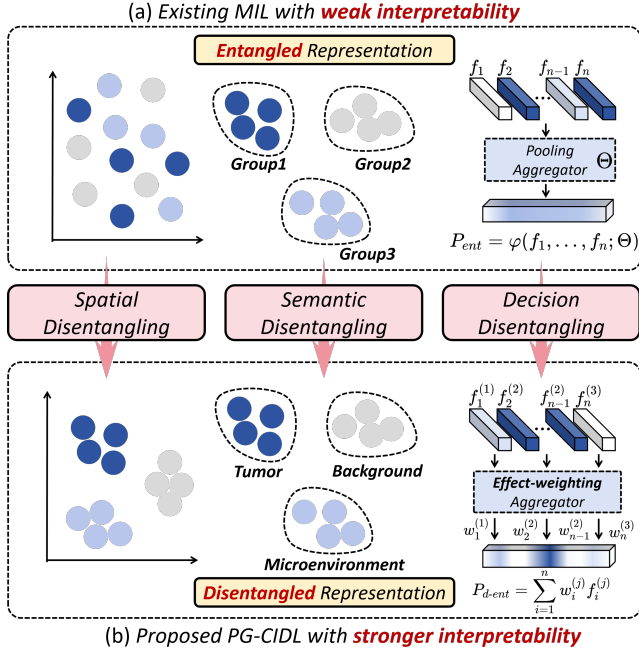


Fig. 1. Motivation of PG-CIDL. (a): Conventional MIL framework with entangled representation has weak interpretability. (b): Proposed PG-CIDL framework with spatial, semantic and decision disentanglement has better interpretability.

cluster-based models [10]–[16] merely approximate instance soft labels and suffer from entangled feature representation, which may highlight background noise and degrade both interpretability and classification performance.

With disentangled semantics, the ultimate decision-making process can still be ambiguous. This decision entanglement results from the fuzzy inter-dependent aggregator in MIL, where instance contributions are determined through pooling or attention mechanisms; see Figure 1. This causes the importance of each patch to be influenced by the global feature distribution, blurring the correspondence between attention weights and true pathological relevance. DGR-MIL [17] utilizes a set of global vectors to represent WSI features, while RRT-MIL [18] re-embeds degraded features via a regional transformer. Causality-based MIL models have been explored to capture instance correlations during decision-making [19]–[22], [22]–[25]. For example, IBMIL [24] addresses the spurious correlations between bags and labels based on the backdoor adjustment, while CaMIL [25] blocks the spurious association between disease and the color by applying the front-door adjustment. MFC-MIL [22] employs an adaptive memory module to simulates causal interventions to mitigate confounders in diagnosis tasks. In general, although these methods tend to refine WSI representation, not only the final decision-making remains ambiguous without specific causal effect weighting, but they lack structural causal model to build disentangled relationships.

To address these entanglement, we introduce PG-CIDL, a three-phase disentangled representation learning framework for interpretable WSI analysis, which enables the model to disentangle spatially, semantically and decision ambiguous representations; see Figure 1. First, we proposed a novel pos-

itive semi-definite latent factor grouping (PSD-LFG) method, which maps spatially entangled instances into a implicit subspace and adaptively partition them into three latent groups. To address semantic entanglement, we develop the cluster-reasoning instance disentangling (CID) in the second phase. By instance probability counterfactual inference, we measure its causal effect, for which features are disentangled by the extent of effects. Finally, the obtained effects are used to re-weighting original feature to get a refined WSI representation via generalized linear weighted summation, mitigating decision entanglement. Through end to end training, our proposed PG-CIDL not only disentangles instances into domain-specific semantics, but also improves the classification performance and interpretability. Our contributions can be summarized as follows:

- We proposed positive semi-definite latent factor grouping for spatial disentanglement, which maps features into latent subspace and provide robust grouping results.
- We introduce cluster-reasoning instance disentangling to identify groups into separate semantics with effects measured by instance probability counterfactual inference.
- To address decision entanglement, we utilize instance effect re-weighting in a generalized linear weighted decision to refine the WSI representation.

II. METHODOLOGY

A. Problem Statement

Assumption: (1): Tumor, microenvironment, and irrelevant background can coexist within each WSI. These weakly-supervised patches meet the criteria for adopting the MIL framework. **(2):** Factors hold causal dependencies in disentangled representation learning (DRL), rather than independence. **(3):** Tumor cells are directly related with pathological grading, while microenvironment interacts with tumor cells, jointly shaping the grading outcome.

MIL Formulation: The goal of WSI-based classification task in MIL framework is to learn a permutation-invariant scoring function [26] \mathcal{F} that maps the set of instances $\mathbf{X} = \{\mathbf{x}_1, \dots, \mathbf{x}_n\}$ to label \mathbf{Y} . The prediction process can be formulated as follows:

$$\hat{\mathbf{Y}} = \mathcal{F}(\mathbf{X}) \quad \text{where} \quad \mathcal{F}(\mathbf{X}) \equiv f(\sigma(\mathcal{A}(\mathbf{X}))) \quad (1)$$

where $\sigma(\cdot)$, $f(\cdot)$ denote the aggregation function, prediction head with softmax normalization, respectively. $\mathcal{A}(\cdot)$ denotes the feature extractor.

WSI-based MIL framework suffer from weak interpretability because of spatial, semantic and decision entanglement. Therefore, we apply DRL to address these entangled dependencies [27].

DRL Formulation: Given the set of instances $\mathbf{X} = \{\mathbf{x}_1, \dots, \mathbf{x}_n\}$, we assume factor tumor (**T**), microenvironment (**E**) and background noise (ϵ) ambiguously generates the whole distribution by function $\Phi(\cdot)$. Thus, DRL aims to disentangle this mapping from given instances to hidden factors $\mathbf{F} = \{\mathbf{h}_1 := \mathbf{T}, \mathbf{h}_2 := \mathbf{E}, \mathbf{h}_3 := \epsilon\}$, i.e.,

$$\mathbf{X} = \Phi(\mathbf{F}) \quad \rightarrow \quad \mathbf{h}_j = \Phi^{-1}(\mathbf{x}_i) \quad (2)$$

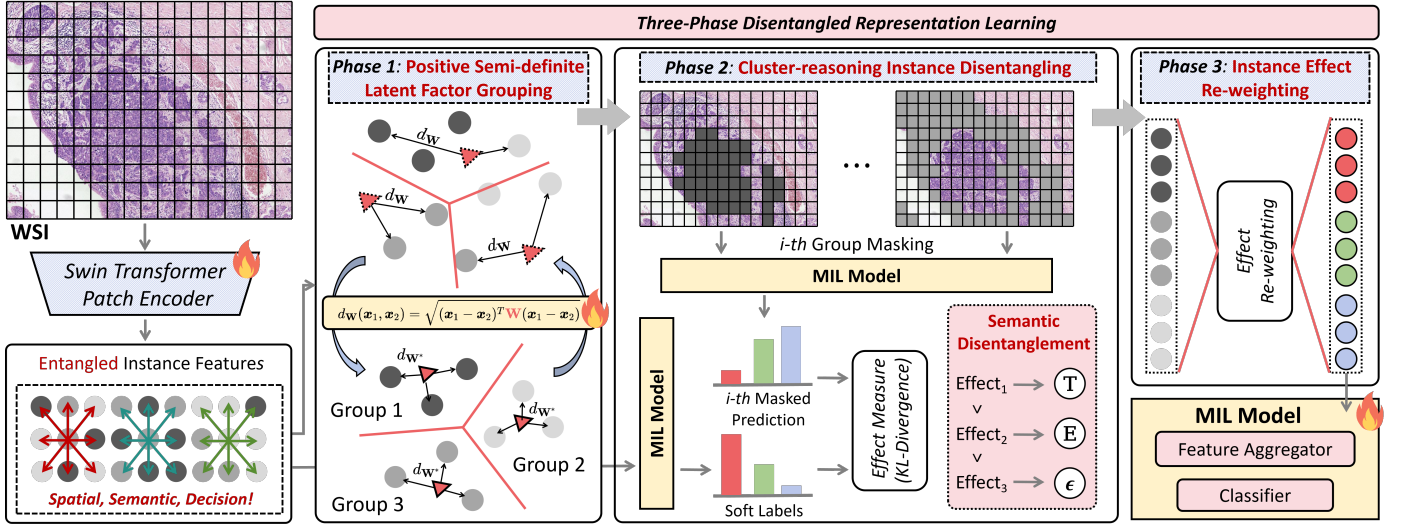


Fig. 2. Overview of **PG-CIDL**. Entangled Features extracted by patch encoder are categorized into three groups via **P**ositive semi-definite latent factor **G**rouping. They are identified into tumor, microenvironment and background factors by **C**luster-reasoning **I**nstance **D**isentangling. End-to-end optimization is performed across all phases for disentangled representation **L**earning with instance effect re-weighted features.

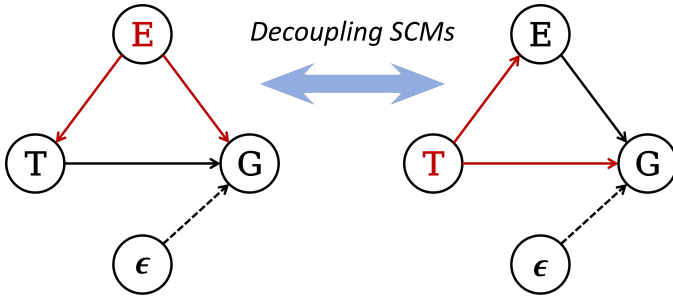


Fig. 3. Two decoupled SCMs for disentangling factors in DRL, where node T is for factor tumor, node E for microenvironment, node G for pathological grading outcome and node ϵ for possible background noise.

In this case, spatial disentanglement can be modeled by expanding the distance \mathcal{D} between each two factors, *i.e.*, maximizing the following,

$$\max_{\mathcal{A}, \Phi} \mathcal{D} = \sum_{j \neq j'} \left\| \mathbb{E}_{\mathbf{x} \sim \mathcal{X}} \left[\mathbb{1}_{h_j} \left(\Phi^{-1}(\mathbf{x}) \right) \mathcal{A}(\mathbf{x}) \right] - \mathbb{E}_{\mathbf{x}' \sim \mathcal{X}} \left[\mathbb{1}_{h_{j'}} \left(\Phi^{-1}(\mathbf{x}') \right) \mathcal{A}(\mathbf{x}') \right] \right\|_2 \quad (3)$$

By the assumption, *factors of variation* in pathological grading are not independent semantics but hold certain causal relations. To address semantic entanglement, we introduce two decoupled SCMs to characterizes these disentangling factors in DRL as prior knowledge. In Figure 3, both two SCMs meet the back-door criterion, which provides a theory for using Pearl's back-door adjustment to estimate the causal effect of one factor by controlling another; see (4). Thus, it guarantees the feasibility of PG-CIDL model desgin.

$$P(\mathbf{G} \mid \text{do}(\mathbf{T})) = \sum_k P(\mathbf{G} \mid \mathbf{T}, \mathbf{E} = e_k) P(\mathbf{E} = e_k) \quad (4)$$

where e_k denotes the controlling option of k instances belonging to factor \mathbf{E} .

Furthermore, we employ information entropy to determine the decision disentanglement. Let $\{\mathbf{x}_1, \dots, \mathbf{x}_n\}$ be random variables of instance in one bag. Then the following theorem holds [4]:

Theorem 1. The joint information entropy can be expressed as $\sum_{i=1}^n H(\mathbf{x}_i)$ iff. \mathbf{x}_i are i.d.d. variables. Furthermore, when they are not i.d.d., we can derive that:

$$\begin{aligned} H(\mathbf{x}_1, \dots, \mathbf{x}_n) &= H(\mathbf{x}_1) + \sum_{i=2}^n H(\mathbf{x}_i \mid \Phi^{-1}(\mathbf{x}_1, \dots, \mathbf{x}_{i-1})) \\ &\leq \sum_{i=1}^n H(\mathbf{x}_i) \end{aligned} \quad (5)$$

Assume that these variables are disentangled into three factors tumor, microenvironment, and background. Let bag \mathbf{X} be partitioned into three subsets with sizes n_1 , $n_2 - n_1$ and $n - n_2$. We can derive that:

$$\begin{aligned} H^*(\mathbf{x}_1, \dots, \mathbf{x}_n) &= w_1 \sum_{i=1}^{n_1} H(\mathbf{x}_i \mid \Phi^{-1}(\mathbf{x}_i) \in \mathbf{h}_1 = \mathbf{T}) \\ &\quad + w_2 \sum_{i=n_1+1}^{n_2} H(\mathbf{x}_i \mid \Phi^{-1}(\mathbf{x}_i) \in \mathbf{h}_2 = \mathbf{E}) \\ &\quad + w_3 \sum_{i=n_2+1}^n H(\mathbf{x}_i \mid \Phi^{-1}(\mathbf{x}_i) \in \mathbf{h}_3 = \epsilon) \\ &\leq H(\mathbf{x}_1) + \sum_{i=2}^n H(\mathbf{x}_i \mid \Phi^{-1}(\mathbf{x}_1, \dots, \mathbf{x}_{i-1})) \\ &\leq \sum_{i=1}^n H(\mathbf{x}_i) \end{aligned} \quad (6)$$

where H^* denotes the correlated information entropy and w_j denotes the instance effects. The weighted summation after

semantic disentanglement only decrease the entropy value compared to the original fuzzy decision. Therefore, the total information entropy of a bag in (6) decreases, which enhance the ability to mitigate decision entanglement.

B. Overview of PG-CIDL

The overall pipeline of PG-CIDL is illustrated in Figure 2. The cropped patches are extracted into feature representations by learnable Swin Transformer [28]. To improve the interpretability of WSI representation within spatially, semantically and decision entangled features, we apply a three-phase disentangled representation learning framework. In phase 1, we perform positive semi-definite latent factor grouping to obtain three semantically ambiguous factors of variation. In phase 2, we disentangle these factors based on instance probability counterfactual inference, where the estimated causal effects categorize them into tumor, microenvironment and background. In phase 3, we refine the original representation by instance effect re-weighting.

C. Positive Semi-definite Latent Factor Grouping

Classic clustering methods with L_p norm with equal weights disregard the interaction and fusion between each two dimensions. As a result, they exacerbate the spatial entanglement of instance features, leading to semantic ambiguity and reduced interpretability. Inspired by the idea of metric learning and deep clustering [29], [30], we proposed a latent factor grouping approach with positive semi-definite constraint to address the limitations.

The general form of metric learning is based on Mahalanobis distance in the following expression.

$$d_{\mathbf{W}}(\mathbf{x}_1, \mathbf{x}_2) = \sqrt{(\mathbf{x}_1 - \mathbf{x}_2)^\top \mathbf{W} (\mathbf{x}_1 - \mathbf{x}_2)} \quad (7)$$

where $\mathbf{W} \in \mathbb{R}^{n \times n}$ is a trainable positive semi-definite matrix and $\mathbf{x}_1, \mathbf{x}_2 \in \mathbb{R}^{n \times 1}$ denote the instance feature representation vectors. If \mathbf{W} is an identity matrix, the distance degrades as standard Euclidean distance.

Positive semi-definite matrix ensures the legality and non-negativity of the metric and facilitates robust metric learning process. Furthermore, compared to diagonal matrix, a general positive semi-definite matrix models more interaction effects among pathological factors, while a diagonal matrix only adjusts the weight of each feature independently.

Fact 1. For any $\mathbf{A} \in \mathbb{R}^{n \times n}$, the matrix $\mathbf{A}^\top \mathbf{A}$ is always positive semi-definite.

Therefore, we replace the L_p norm with the adaptive distance $d_{\mathbf{W}}(\cdot, \cdot)$ and ensure $\mathbf{W} \succeq 0$ by parameterizing $\mathbf{W} = \mathbf{A}^\top \mathbf{A}$, $\mathbf{A} \in \mathbb{R}^{r \times n}$, where $r < n$ ensures a low-rank structure for easier computation. By incorporating optimal $\mathbf{W}^* = \mathbf{A}^{*\top} \mathbf{A}^*$ into KMeans ($k = 3$, Figure 2) we can also assume that PSD-LFG maps the distance into a latent subspace in (8), where we can perform more robust and accurate clustering results, thus alleviating spatial entanglement.

$$\begin{aligned} d_{\mathbf{W}^*}(\mathbf{x}_1, \mathbf{x}_2) &= \sqrt{(\mathbf{x}_1 - \mathbf{x}_2)^\top \mathbf{A}^{*\top} \mathbf{A}^* (\mathbf{x}_1 - \mathbf{x}_2)} \\ &= \|\mathbf{A}^* (\mathbf{x}_1 - \mathbf{x}_2)\|_2 \end{aligned} \quad (8)$$

Algorithm 1 Cluster-reasoning Instance Disentangling and Instance Effect Re-weighting in PG-CIDL

Input: Instance groups $\mathbf{Z} = \{\mathbf{Z}_1, \mathbf{Z}_2, \mathbf{Z}_3\}$; each \mathbf{Z}_k belongs to one of the factors TC, ME and BG.
Output: Final bag feature $\mathbf{Z}_{\text{final}}$ and factor map `factor`

```

1:  $P_v \leftarrow f(\sigma(\mathbf{Z}))$  ▷ vanilla prediction
2: for  $k = 1$  to 3 do
3:    $\mathbf{Z}_{\setminus k} \leftarrow \{\mathbf{Z}_j : j \neq k\}$ 
4:    $P_k \leftarrow f(\sigma(\mathbf{Z}_{\setminus k}))$ 
5:    $D_k \leftarrow D_{\text{KL}}(P_v \| P_k)$ 
6: end for
7:  $\{w_k\}_{k=1}^3 \leftarrow \text{Normalize}(\{D_k\})$ 
8:  $\text{order} \leftarrow \text{argsort}(\{w_k\}, \text{descend})$ 
9:  $\text{factor}[\text{TC}] \leftarrow \mathbf{Z}_{\text{order}[1]}, \dots, \text{factor}[\text{BG}] \leftarrow \mathbf{Z}_{\text{factor}[3]}$ 
10:  $\mathbf{Z}_{\text{final}} \leftarrow \text{mean}(\sum_{k=1}^3 w_k \mathbf{Z}_k)$ 
11: return  $\mathbf{Z}_{\text{final}}, \text{factor}$ 

```

D. Cluster-reasoning Instance Disentangling

Based on the results from Phase 1, we obtained three latent yet semantically entangled instance groups. According to the SCMs introduced before as prior knowledge, we proposed CID, which leverages counterfactual inference to estimate the causal effects within factors, thereby disentangling ambiguous semantics and improving the model's interpretability and generalization. Figure 2 and Algorithm 1 intuitively present the idea of CID, which involves the following three steps.

Group Masking: Let $\mathcal{A}(\mathbf{X}) = \mathbf{Z} \rightarrow \{\mathbf{Z}_1, \mathbf{Z}_2, \mathbf{Z}_3\}$ be three instance groups from phase 1. The intervention sets $\text{do}(\mathbf{Z}_{\setminus k})$ as

$$\mathbf{Z}_{\setminus k} = \mathbf{Z} \setminus \mathbf{Z}_k, \quad k = 1, 2, 3 \quad (9)$$

This masking severs all back-door paths through \mathbf{Z}_k and thus isolates its causal effect. Then the prediction under that intervention is

$$P_k = f(\sigma(\mathbf{Z} | \text{do}(\mathbf{Z}_{\setminus k}))) \quad (10)$$

where we consider the counterfactual of factor \mathbf{Z}_k as $\mathbf{Z}_{\setminus k}$ that masking \mathbf{Z}_k . This masked prediction serve as an important component for causal effect measurement.

Effect Measurement: Let $P_v = f(\sigma(\mathbf{Z}))$ be the vanilla prediction without any intervention, which serves as the reference and soft labels for comparison. We regard P_v as the target distribution and P_k as the ones approximate the target. Due to this asymmetry, we employ Kullback-Leibler divergence to calculate pairwise difference D_k as effects in (11).

$$D_k = D_{\text{KL}}(P_v \| P_k) = \sum_z P_v(z) \log\left(\frac{P_v(z)}{P_k(z)}\right) \quad (11)$$

where D_k reveals how much the masked group of instances influence the original prediction.

Semantic Disentangling: A larger D_k suggests a more pathologically important group (e.g. tumor), while a smaller one indicates irrelevant groups (e.g. background and microenvironment). Consequently, we can causally identify the *factors of variation* of each group by tumor, microenvironment and background based on the previous assumption; see Algorithm 1.

TABLE I

PERFORMANCE COMPARISON OF WSI CLASSIFICATION ON MULTICENTRE DATASETS WITH SWIN-T PRETRAINED FEATURES.

Models	AMU-CSCC			AMU-LSCC			CAMELYON16			DHMC-LUNG		
	ACC	WF1	AUC	ACC	WF1	AUC	ACC	WF1	AUC	ACC	WF1	AUC
ABMIL	0.8302	0.8073	0.9547	0.6739	0.6701	0.7888	0.7429	0.7314	0.7918	0.7333	0.7333	0.8123
CLAM-SB	0.8302	0.7974	0.9581	0.6957	0.6933	0.8367	0.7429	0.7229	0.7478	0.7556	0.7551	0.7783
CLAM-MB	0.8774	0.8788	0.9336	0.6812	0.6811	0.8031	0.7429	0.7314	0.7339	0.7333	0.7333	0.7684
TransMIL	0.8868	0.8860	0.9521	0.8261	0.8276	0.9021	0.7429	0.7437	0.6898	0.7333	0.7333	0.8084
DTFD-MIL	0.8113	0.7682	0.9036	0.5435	0.5186	0.7245	0.7143	0.6972	0.7306	0.6889	0.6671	0.6983
IBMIL-DS	0.7830	0.7421	0.8881	0.6377	0.6374	0.7672	0.7429	0.7437	0.7037	0.6889	0.6889	0.7091
ILRA-MIL	0.8491	0.8423	0.9123	0.6884	0.6792	0.8048	0.7714	0.7687	0.7306	0.7778	0.7767	0.8074
S4MIL	0.8491	0.8163	0.9605	0.7971	0.7970	0.8845	0.7429	0.7429	0.7322	0.7111	0.7052	0.7007
FRMIL	0.8113	0.7668	0.8990	0.6377	0.6383	0.8020	0.7143	0.6972	0.6914	0.7111	0.7114	0.7442
DGR-MIL	0.8868	0.8858	0.9613	0.8188	0.8192	0.9147	0.8286	0.8265	0.8253	0.8000	0.8002	0.7886
ACMIL-MHA	0.9057	0.9070	0.9701	0.8551	0.8568	0.9219	0.8000	0.8007	0.7331	0.6889	0.6671	0.6849
RRT-MIL	0.8585	0.8560	0.9265	0.7681	0.7684	0.8732	0.7143	0.7109	0.7608	0.7778	0.7746	0.7521
MFC-MIL	0.8962	0.8940	0.9723	0.8261	0.8268	0.9126	0.7714	0.7714	0.7208	0.7778	0.7767	0.7931
PG-CIDL (ours)	0.9434	0.9450	0.9859	0.9275	0.9264	0.9719	0.8857	0.8821	0.9282	0.8444	0.8413	0.8820

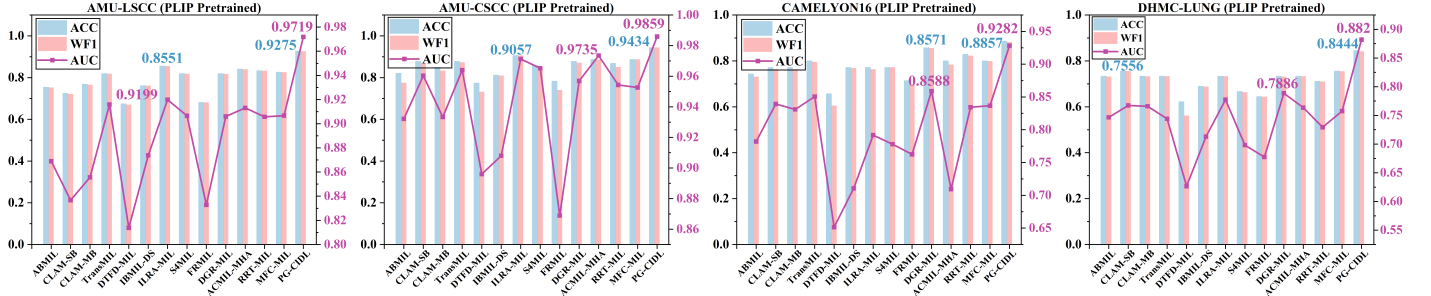


Fig. 4. Performance comparison on multicentre datasets with PLIP pretrained features.

E. Instance Effect Re-weighting and Optimization

We normalize each “leave-one-out” prediction divergence D_k to get approximate effect $w_k = \frac{D_k}{\sum_j D_j}$ and perform effects re-weighting to refine the representation.

$$\mathbf{Z}_{\text{final}} = \text{mean} \left(\sum_{k=1}^3 w_k \mathbf{Z}_k \right) \quad (12)$$

which can reflect how the previously disentangled instances effect the final WSI representation and mitigating decision entanglement. Finally, we perform end-to-end optimization across all stages to learn more task-related, interpretable and generalized feature representations. Specifically, the loss function is formulated as follows:

$$\begin{aligned} \mathcal{L} &= \mathcal{L}_{ce}(f(\sigma(\mathbf{Z}_{\text{final}}))) - \gamma \cdot d_{\text{reg}} \\ d_{\text{reg}} &= d_{\mathbf{W}} \left(\text{mean}(\mathbf{Z}^{\text{TC}}), \text{mean}(\mathbf{Z} \setminus \mathbf{Z}^{\text{TC}}) \right) \end{aligned} \quad (13)$$

where \mathcal{L}_{ce} denotes the cross entropy. Since KMeans algorithm is not normally differentiable, this group-separation regularizer d_{reg} that encourages the mean of the tumor group to move away from the mean of all other instances helps to optimize the trainable matrix \mathbf{W} by computing the gradients $\frac{\partial \mathcal{L}}{\partial \mathbf{A}}$.

III. EXPERIMENTAL RESULTS

A. Datasets and Setup

Datasets: To validate PG-CIDL for diagnosis and sub-typing tasks, we conduct extensive experiments on two public datasets and two private datasets. Two private WSI datasets were collected from Army Medical University, where **AMU-LSCC** is for laryngeal squamous cell carcinoma pathological grading and **AMU-CSCC** is for cervical squamous cell carcinoma. AMU-LSCC dataset includes 342 whole slide images that was divided by a 6:4 training-validation ratio for each category. Specially Grade I contains a total of 89 WSIs, Grade II contains 152 WSIs and Grade III includes 101 WSIs. AMU-CSCC dataset includes 262 whole slide images, where Grade I contains a total of 27 WSIs, Grade II contains 127 WSIs and Grade III includes 108 WSIs. Two chosen public datasets are **CAMELYON16** for breast cancer lymph node metastasis detection [31] and **DHMC-LUNG** [32] for lung adenocarcinoma classification.

Compared MIL Models: We implemented eleven state-of-the-art (SOTA) MIL models for comparison. They are ABMIL [2], CLAMs [13], TransMIL [4], DTFD-MIL [33], ILRA-MIL [34], IBMIL [24], S4MIL [35], DGRMIL [17], FRMIL [36], ACMIL [3], RRT-MIL [18] and MFC-MIL [22]. Moreover, we report Accuracy, Area Under Curve (AUC), and Weighted F1-score for evaluation metrics.

Implementation: For comprehensive comparison, we extract

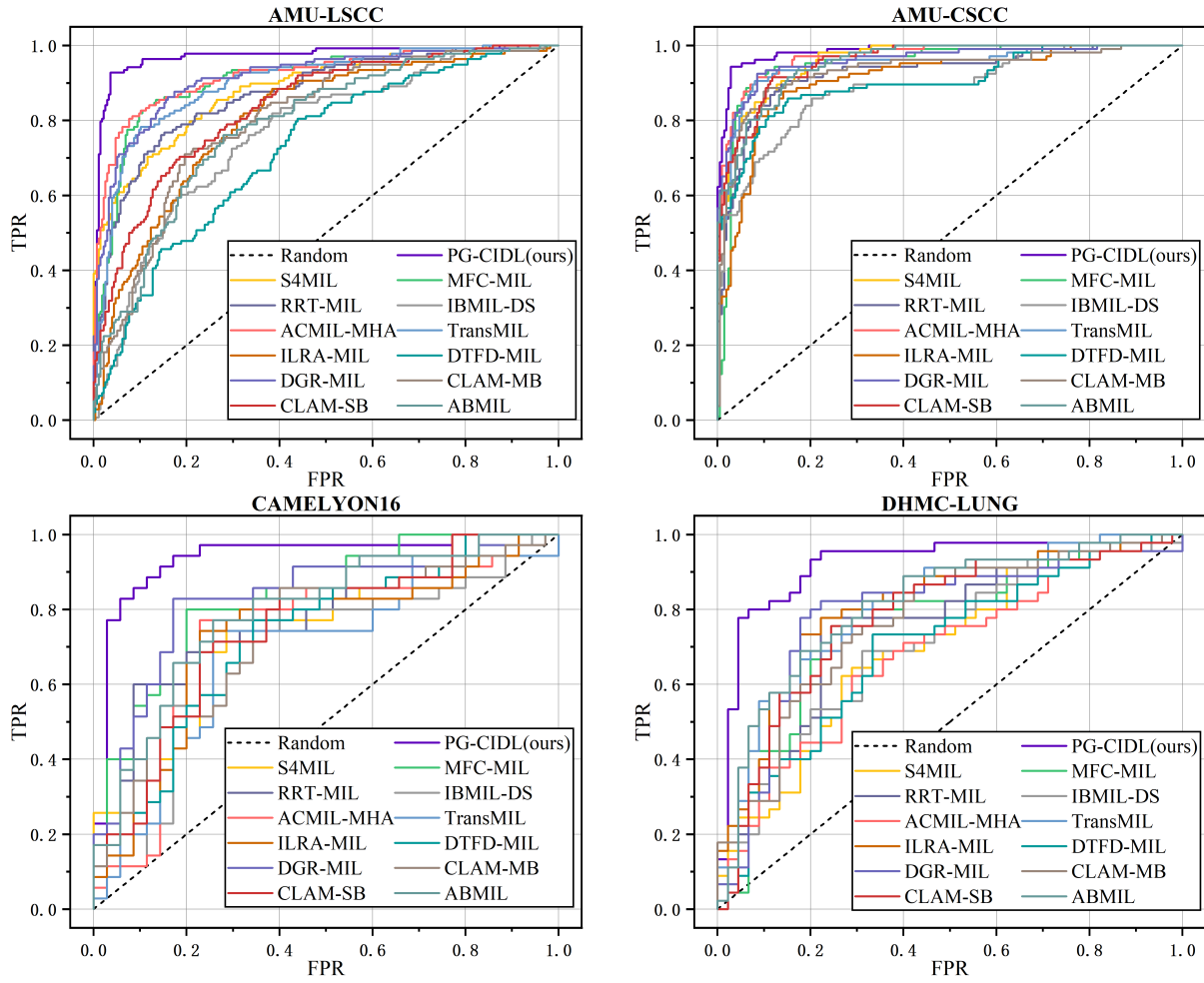


Fig. 5. ROC plots' comparison on multicentre datasets.

features with Swin Transformer [28] pretrained on ImageNet-11k and PLIP [37] pretrained on OpenPath, respectively. We utilize Rmsprop optimizer for training. Models on two private datasets were trained with a batch size of 2 and 100 epochs. For public datasets, batch size is set 1. The random seed was fixed 0 across all stages. The input resolution of PG-CIDL is $96 \times 96 \times 3$. The learning rate schedule was: 1×10^{-5} for epochs 1–50, 5×10^{-6} for epochs 51–75, and 1×10^{-6} for epochs 76–100. The hyper-parameter γ in loss function was set 0.1. Patches were grid cropped from each WSI in 10x magnification and we filtered out instances with blank areas.

Computational Specs: Experiments were conducted on Ubuntu 22.04 with x86.64 architecture with four *NVIDIA A10 Tensor Core 24GB*. For computational framework and library versions: we use PyTorch 2.6.0, CUDA 12.4, cuDNN 9.1. For training CAMELYON16 specifically, the peak memory usage is 13GB each GPU at one batch. In terms of model inference, it takes 0.123s per WSI for feature extraction and 0.355s for three-phase DRL.

B. Comparison with SOTA Methods

For diagnostic tasks like CAMELYON16 (tumor vs. normal), WSIs may exhibit varying differentiation states, but

rather than discussed factors. Yet, they can be more accurately diagnosed when patches are categorized with causal relevance. Table I and Figure 4 present the performance of SOTA methods on multicentre datasets.

The results suggest that our PG-CIDL outperforms all SOTA models across all three evaluation metrics and four benchmarks. For features pretrained on ImageNet-11k, while ACMIL-MHA achieves the second-best classification performance on AMU-LSCC, our model improves the ACC and AUC by 7.24% and 5.00%, respectively. On CAMELYON16 dataset, the improvement is 5.71% and 10.29% compared to DGR-MIL. AMU-CSCC and DHMC-LUNG have also seen the similar trend that our proposed PG-CIDL achieves the best classification performance. Although two private datasets suffer from class imbalance, the reported Weighted-F1 scores also show the similar improvement with 3.80% and 6.96% of gains respectively. Figure 5 illustrates the curve of PG-CIDL lies above all the other curves and suggests the largest area under the curve (AUC), which implies that our PG-CIDL achieves the highest predictive confidence among all SOTA models.

In Figure 4, we notice that incorporating features extracted by PLIP pretrained on WSIs, most models fail to exhibit a significant improvement. Specifically, we only observe a

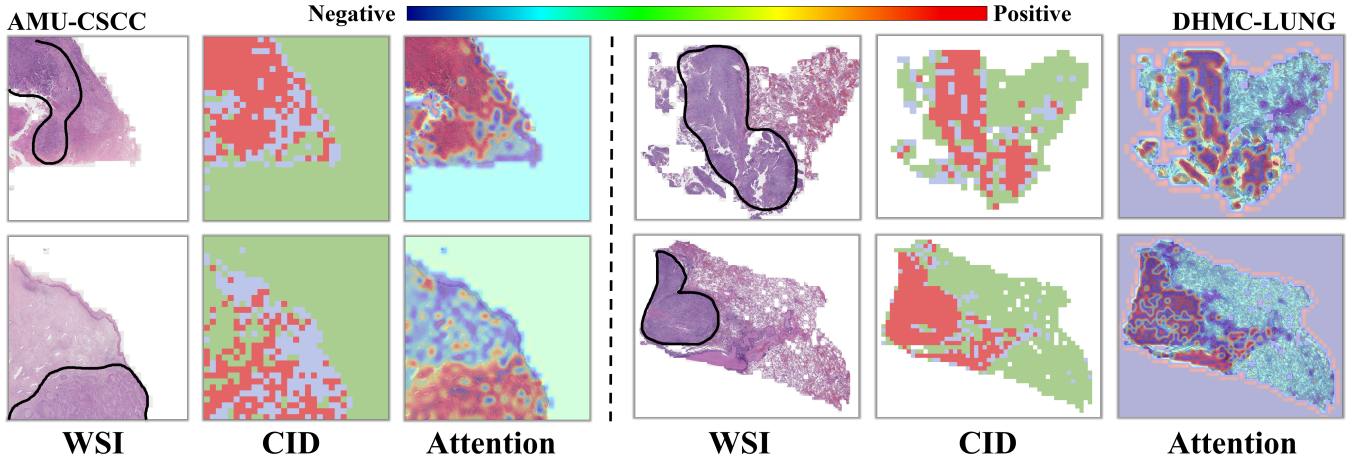


Fig. 6. Visualization results on AMU-CSCC and DHMC-LUNG. The first column is original WSI with pathologist-annotated tumor boundaries. The second column is the labeled regions after CID, where red, blue, green denote factor tumor, environment and background respectively. The last column is the attention heatmap corresponding to its category.

TABLE II

ABLATION EXPERIMENTS ON DIFFERENT CLUSTERING METHODS IN PG-CIDL. THE BASELINE MODEL IS VANILLA SWIN TRANSFORMER.

Models (AMU-CSCC)	ACC	AUC
MFC-MIL	0.8962	0.9723
ACMIL-MHA	0.9057	0.9701
baseline	0.8868	0.9778 ↑
PG-CIDL w/o PSD-LFG	0.8962 ↑	0.9641 ↓
PG-CIDL w/o CID	0.8868	0.9825
PG-CIDL	0.9434 ↑	0.9859 ↑

TABLE III

ABLATION EXPERIMENTS ON DIFFERENT METRICS IN CID.

Metrics in CID	AMU-CSCC		CAMELYON16	
	ACC	AUC	ACC	AUC
Cosine distance	0.9151	0.9776	0.6857	0.7771
Hellinger distance	0.9245	0.9795	0.8857	0.9151
JS divergence	0.9434	0.9849	0.8571	0.8882
KL divergence (ours)	0.9434	0.9859	0.8857	0.9282

moderate increase on CAMELYON16, with the second-best ACC rising from 82.86% to 85.71% and AUC from 82.53% to 85.88%. For detailed information, please refer to the Supplementary Material. Despite this, our PG-CIDL remains superior to all compared SOTA models. We attribute this achievement to the advantages of refined representation from PSD-LFG and CID in our disentangled representation learning framework, which will be validated in the following sections.

C. Ablation Experiments

To validate the effectiveness of components proposed in PG-CIDL, we conducted extensive ablation experiments. In Table II, we choose the baseline model as a fully supervised mean-pooling framework, which outperforms the second-best MFC-MIL on AMU-CSCC with 0.55% AUC improvement but ACC drops 1.89% compared to ACMIL-MHA. In general, It suggests that end-to-end learning can learn task-related feature

representation that leads to better classification performance.

We simply consider three factors due to the motivation that for most WSI diagnosis tasks, the main variability is between tumor, its microenvironment and background. Larger numbers of groups are needed for more complex tasks [10]. We validate PSD-LFG by replacing with L2-KMeans, we observe a 0.94% improvement in ACC and a 1.37% drop in AUC. Since instance grouping is the basis for counterfactual inference, an inaccurate and entangled grouping result may introduce epistemic errors into the causal graph and disentangling process. Incorporating PSD-LFG, PG-CIDL then ensures a robust reasoning process with disentangled and refined representation, leading to optimal classification performance. Besides, we test the performance of using grouping strategy alone with fixed attention weighting. It shows that our PG-CIDL degrades without causal effects re-weighting from CID. Instead, combining these two components improves both ACC and AUC.

Moreover, Table III reports the performance of different metrics employed in CID module. It indicates that cosine distance is the least suitable metric. As a symmetric version of KL, the JS divergence achieves comparable performance with only a 0.1% drop in ACC on the AMU-CSCC. Overall, these results demonstrate that incorporating KL divergence in CID module yields superior performance.

To further validate the generalization capability of PG-CIDL, we performed end-to-end training on selected 7 SOTA MIL models for fairer comparison. In Table IV, these models achieve slightly better performance compared to two-stage training. However, our proposed PG-CIDL with disentangled representation still outperform these MIL models. It especially improved the second-best mACC by 8.69% and AUC by 4.46%.

D. Visualization of Model Interpretability

To validate whether our model managed to identity instance features into three disentangled factors, we provide visualization results of our PG-CIDL on AMU-CSCC, AMU-

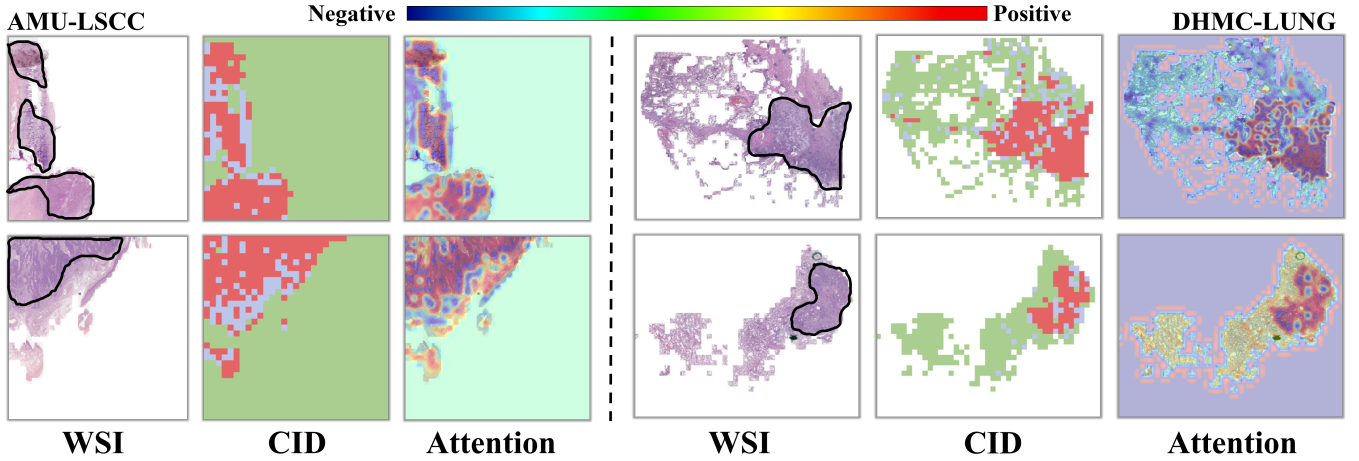


Fig. 7. Extra visualization results on AMU-LSCC and DHMC-LUNG.

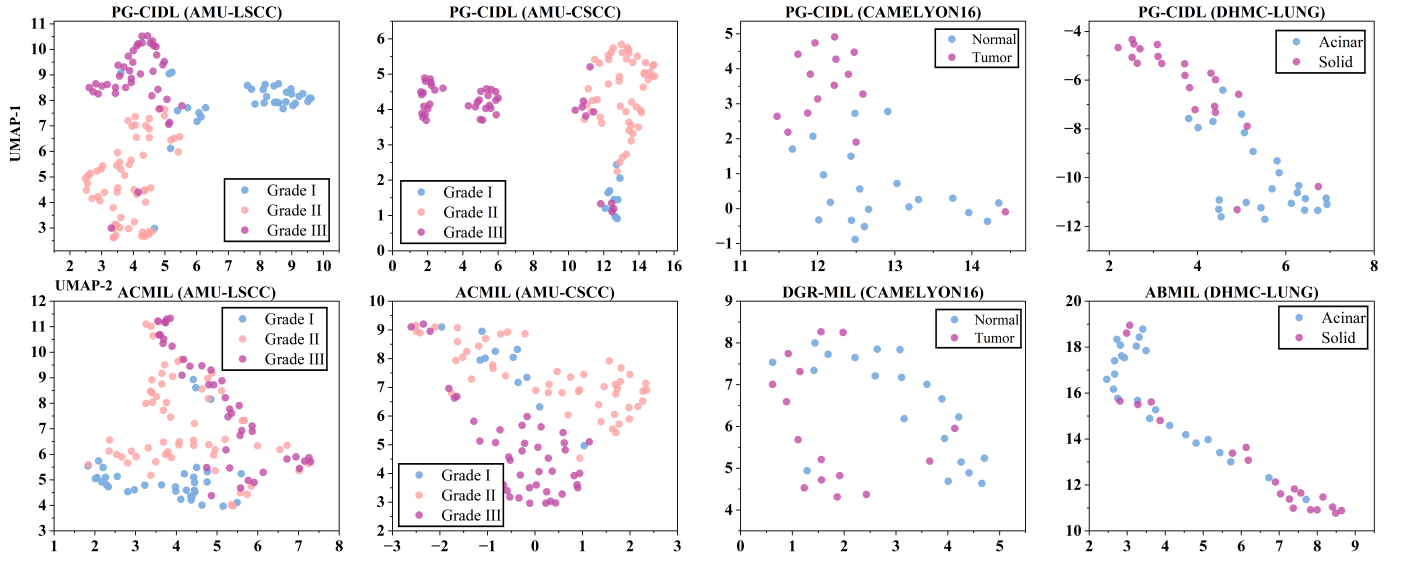


Fig. 8. 2-D feature representation with spatial disentanglement on multicentre datasets.

TABLE IV
END-TO-END PERFORMANCE COMPARISON OF PG-CIDL AND OTHER
SOTA MODELS ON LSCC.

End-to-End	mAcc	WF1	AUC
ABMIL(Linear)	0.7826	0.7791	0.9120
TransMIL	0.8188	0.8205	0.9116
DGR-MIL	0.8188	0.8165	0.9273
ACMIL-MHA	0.8406	0.8414	0.9252
ILRA-MIL	0.8116	0.8119	0.9198
RRT-MIL	0.7826	0.7815	0.9038
MFC-MIL	0.8116	0.8112	0.9115
PG-CIDL (ours)	0.9275	0.9264	0.9719

LSCC and DMHC-LUNG. In Figure 6 and Figure 7. We can see that both disentangled factors and attention heatmaps highlight the area that are highly consistent with pathologists' annotations. More specifically, the clustering and labeling

results from CID reflect the model's active interpretability, as it disentangles semantically ambiguous features and explicitly groups regions with tumor, microenvironment and background before final prediction, mirroring a real-world diagnostic workflow. Meanwhile, the attention heatmaps highlight the most contributive regions for classification, revealing the model's passive interpretability.

Overall, these two kinds of interpretability demonstrate that PG-CIDL not only learns more interpretable and task-relevant representations, but also aligns well with clinical reasoning, offering a comprehensive explanation of predictions. It also implies a potential paradigm for weakly supervised semantic segmentation.

E. Capability of Feature Representation

We utilize UMAP [38] to visualize feature representation in 2-D space. In Figure 8, we can see that our proposed PG-CIDL show less entanglement within feature distributions,

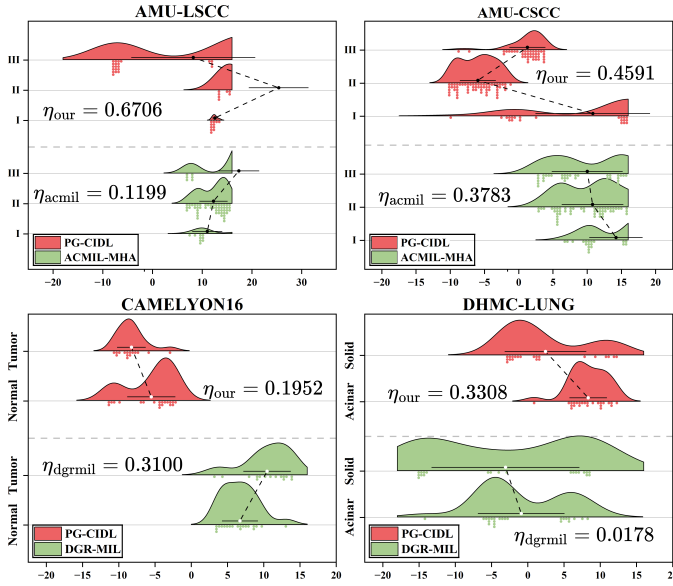


Fig. 9. ANOVA plots on four datasets where η_* denote the value of effect size.

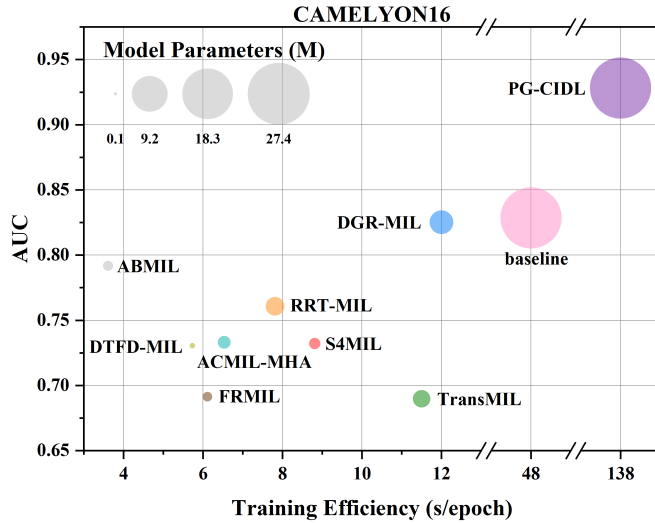


Fig. 10. Model complexity vs. performance.

while other sub-optimal models without spatial disentanglement show more feature overlaps. It not only implies that PG-CIDL disentangles feature spatially, but it also has superior ability to distinguish feature related to corresponding grading results.

An effective classification model should be able to capture and fit the differences among pathological patterns. To validate this assumption, we visualize the final layer feature representation of each model using UMAP in 1-D space. Figure 9 shows the analysis of variance (ANOVA) with effect size metrics (η^2).

The effect size in ANOVA quantifies the proportion of variance in the dependent variable explained by the group labels. A larger effect size suggests a stronger ability of

the model to capture and distinguish differences between classes. In Figure 9, PG-CIDL models the distinct distributions within different categories, while ACMIL and DGR-MIL tend to overlap. It has larger effect size 0.6706, 0.4591, 0.3308 compared to the second-best models on AMU-CSCC, AMU-LSCC and DHMC-LUNG, respectively. Although DGR-MIL on CAMELYON16 exhibit effect size 1.5 times larger, PG-CIDL still remains a considerable amount of η^2 . Therefore, our proposed PG-CIDL exhibits better feature representation ability in general, which directly implies that our model is capable of address all three aspects of entanglement to obtain more explainable and generalized representation.

F. Model Complexity Analysis

End-to-end learning for WSI analysis is considered to be computationally intensive, accordingly receiving limited exploration. However, our findings suggest that its actual computational demand has been overestimated. In Supplementary Material, we present detailed computational specs. In Figure 10 we present comparison of complexity vs. performance on CAMELYON16 of batch size 1.

Specifically, our PG-CIDL contains 27.50M parameters significantly more than existing models, which range from 0.199M (DTFD-MIL) to 4.075M (DGR-MIL). This leads to a longer training time per epoch for PG-CIDL (138s), compared to 12.0s for DGR-MIL, the most computationally demanding among the SOTA models. Although our PG-CIDL approach increases training time ten times larger, the computational cost is relatively accepted. It allows the model to learn highly task-specific feature representations, resulting in better classification accuracy and enhanced interpretability.

IV. CONCLUSION

WSI-based pathological grading is the golden standard for clinical diagnosis and prognosis. As one of the main-stream frameworks for WSI classification, multi-instance learning models suffer from weak interpretability and generalizability caused by spatially, semantically and decision entangled representations. Guided by a prior structural causal model, we proposed a three-phase disentangled representation learning framework PG-CIDL, followed by positive semi-definite latent factor grouping, counterfactual inference-based cluster-reasoning instance disentangling and instance effect re-weighting. In this case, our PG-CIDL decomposes the entangled features into three causally relevant factors, namely tumor, microenvironment, and background, and refines them to derive a more interpretable WSI representation. Extensive experiments on multicentre datasets demonstrate that our PG-CIDL not only achieves superior classification performance, but exhibits strong capability of disentangled feature representation, interpretability and generalizability. Our study also explored end-to-end learning for WSIs. Unlike conventional two-step models that rely on offline features or separate clustering pipelines, our unified framework optimizes feature across all stages. This leads to more task-relevant and interpretable representations.

REFERENCES

- [1] N. Kumar, R. Gupta, and S. Gupta, "Whole slide imaging (wsi) in pathology: current perspectives and future directions," *Journal of digital imaging*, vol. 33, no. 4, pp. 1034–1040, 2020.
- [2] M. Ilse, J. Tomczak, and M. Welling, "Attention-based deep multiple instance learning," in *International Conference on Machine Learning*. PMLR, 2018, pp. 2127–2136.
- [3] Y. Zhang, H. Li, Y. Sun, S. Zheng, C. Zhu, and L. Yang, "Attention-challenging multiple instance learning for whole slide image classification," in *European Conference on Computer Vision*. Springer, 2024, pp. 125–143.
- [4] Z. Shao, H. Bian, Y. Chen, Y. Wang, J. Zhang, X. Ji *et al.*, "Transmil: Transformer based correlated multiple instance learning for whole slide image classification," *Advances in neural information processing systems*, vol. 34, pp. 2136–2147, 2021.
- [5] B. Li, Y. Li, and K. W. Eliceiri, "Dual-stream multiple instance learning network for whole slide image classification with self-supervised contrastive learning," in *Proceedings of the IEEE/CVF conference on computer vision and pattern recognition*, 2021, pp. 14 318–14 328.
- [6] M. Ilse, J. Tomczak, and M. Welling, "Attention-based deep multiple instance learning," in *International conference on machine learning*. PMLR, 2018, pp. 2127–2136.
- [7] R. J. Chen, M. Y. Lu, W.-H. Weng, T. Y. Chen, D. F. Williamson, T. Manz, M. Shady, and F. Mahmood, "Multimodal co-attention transformer for survival prediction in gigapixel whole slide images," in *Proceedings of the IEEE/CVF international conference on computer vision*, 2021, pp. 4015–4025.
- [8] N. Pawlowski, D. Coelho de Castro, and B. Glocker, "Deep structural causal models for tractable counterfactual inference," *Advances in neural information processing systems*, vol. 33, pp. 857–869, 2020.
- [9] A. Renshaw, "Diagnostic histopathology of tumors," 2014, forthcoming.
- [10] A. H. Song, R. J. Chen, T. Ding, D. F. Williamson, G. Jaume, and F. Mahmood, "Morphological prototyping for unsupervised slide representation learning in computational pathology," in *Proceedings of the IEEE/CVF Conference on Computer Vision and Pattern Recognition*, 2024, pp. 11 566–11 578.
- [11] A. Liu, T. Li, J. Cai, and S. S. V. Vajrjala, "Fuzzymil: Decoupling pathological phenotypes through deep fuzzy clustering for efficient whole slide image analysis," in *ICASSP 2025-2025 IEEE International Conference on Acoustics, Speech and Signal Processing (ICASSP)*. IEEE, 2025, pp. 1–5.
- [12] Y. Chen, T. H. Chan, G. Yin, Y. Jiang, and L. Yu, "cdp-mil: Robust multiple instance learning via cascaded dirichlet process," in *European conference on computer vision*. Springer, 2024, pp. 232–250.
- [13] M. Y. Lu, D. F. Williamson, T. Y. Chen, R. J. Chen, M. Barbieri, and F. Mahmood, "Data-efficient and weakly supervised computational pathology on whole-slide images," *Nat. Biomed. Eng.*, vol. 5, no. 6, pp. 555–570, 2021.
- [14] J. Jin, S. Wang, Z. Dong, X. Liu, and E. Zhu, "Deep incomplete multi-view clustering with cross-view partial sample and prototype alignment," in *Proceedings of the IEEE/CVF conference on computer vision and pattern recognition*, 2023, pp. 11 600–11 609.
- [15] W. Yan, Y. Zhang, C. Lv, C. Tang, G. Yue, L. Liao, and W. Lin, "Gcfagg: Global and cross-view feature aggregation for multi-view clustering," in *Proceedings of the IEEE/CVF conference on computer vision and pattern recognition*, 2023, pp. 19 863–19 872.
- [16] Y. Zheng, K. Wu, J. Li, K. Tang, J. Shi, H. Wu, Z. Jiang, and W. Wang, "Partial-label contrastive representation learning for fine-grained biomarkers prediction from histopathology whole slide images," *IEEE Journal of Biomedical and Health Informatics*, 2024.
- [17] W. Zhu, X. Chen, P. Qiu, A. Sotiras, A. Razi, and Y. Wang, "Dgr-mil: Exploring diverse global representation in multiple instance learning for whole slide image classification," in *European Conference on Computer Vision*. Springer, 2024, pp. 333–351.
- [18] W. Tang, F. Zhou, S. Huang, X. Zhu, Y. Zhang, and B. Liu, "Feature re-embedding: Towards foundation model-level performance in computational pathology," in *Proceedings of the IEEE/CVF Conference on Computer Vision and Pattern Recognition*, 2024, pp. 11 343–11 352.
- [19] X. Wu, H. Wang, and H. Wu, "Causal attention multiple instance learning for whole slide image classification," in *The 16th Asian Conference on Machine Learning (Conference Track)*, 2024.
- [20] R. Guo, Z. Xie, C. Zhang, and X. Qian, "Causality-enhanced multiple instance learning with graph convolutional networks for parkinsonian freezing-of-gait assessment," *IEEE Transactions on Image Processing*, vol. 33, pp. 3991–4001, 2024.
- [21] T. Nan, Y. Ding, H. Quan, D. Li, L. Li, G. Zhao, and X. Cui, "Establishing causal relationship between whole slide image predictions and diagnostic evidence subregions in deep learning," *arXiv preprint arXiv:2407.17157*, 2024.
- [22] X. Cui, W. Chen, and J. Su, "A multiscale frequency domain causal framework for enhanced pathological analysis," in *The Thirteenth International Conference on Learning Representations*, 2025.
- [23] W. Lin, Z. Zhuang, L. Yu, and L. Wang, "Boosting multiple instance learning models for whole slide image classification: A model-agnostic framework based on counterfactual inference," in *Proceedings of the AAAI Conference on Artificial Intelligence*, vol. 38, no. 4, 2024, pp. 3477–3485.
- [24] T. Lin, Z. Yu, H. Hu, Y. Xu, and C.-W. Chen, "Interventional bag multi-instance learning on whole-slide pathological images," in *Proceedings of the IEEE/CVF Conference on Computer Vision and Pattern Recognition*, 2023, pp. 19 830–19 839.
- [25] K. Chen, S. Sun, and J. Zhao, "Camil: Causal multiple instance learning for whole slide image classification," in *Proceedings of the AAAI Conference on Artificial Intelligence*, vol. 38, no. 2, 2024, pp. 1120–1128.
- [26] M. Zaheer, S. Kottur, S. Ravanbakhsh, B. Poczos, R. R. Salakhutdinov, and A. J. Smola, "Deep sets," *Advances in neural information processing systems*, vol. 30, 2017.
- [27] X. Wang, H. Chen, S. Tang, Z. Wu, and W. Zhu, "Disentangled representation learning," *IEEE Transactions on Pattern Analysis and Machine Intelligence*, vol. 46, no. 12, pp. 9677–9696, 2024.
- [28] Z. Liu, Y. Lin, Y. Cao, H. Hu, Y. Wei, Z. Zhang, S. Lin, and B. Guo, "Swin transformer: Hierarchical vision transformer using shifted windows," in *Proceedings of the IEEE/CVF international conference on computer vision*, 2021, pp. 10 012–10 022.
- [29] M. Caron, P. Bojanowski, A. Joulin, and M. Douze, "Deep clustering for unsupervised learning of visual features," in *Proceedings of the European conference on computer vision (ECCV)*, 2018, pp. 132–149.
- [30] H. Tang, K. Chen, and K. Jia, "Unsupervised domain adaptation via structurally regularized deep clustering," in *Proceedings of the IEEE/CVF conference on computer vision and pattern recognition*, 2020, pp. 8725–8735.
- [31] B. E. Bejnordi, M. Veta, P. J. Van Diest, B. Van Ginneken, N. Karssemeijer, G. Litjens, J. A. Van Der Laak, M. Hermesen, Q. F. Manson, M. Balkenhol *et al.*, "Diagnostic assessment of deep learning algorithms for detection of lymph node metastases in women with breast cancer," *Jama*, vol. 318, no. 22, pp. 2199–2210, 2017.
- [32] J. W. Wei, L. J. Tafe, Y. A. Linnik, L. J. Vaickus, N. Tomita, and S. Hassanpour, "Pathologist-level classification of histologic patterns on resected lung adenocarcinoma slides with deep neural networks," *Scientific reports*, vol. 9, no. 1, p. 3358, 2019.
- [33] H. Zhang, Y. Meng, Y. Zhao, Y. Qiao, X. Yang, S. E. Coupland, and Y. Zheng, "Dtfd-mil: Double-tier feature distillation multiple instance learning for histopathology whole slide image classification," in *Proceedings of the IEEE/CVF Conference on Computer Vision and Pattern Recognition*, 2022, pp. 18 802–18 812.
- [34] J. Xiang and J. Zhang, "Exploring low-rank property in multiple instance learning for whole slide image classification," in *The Eleventh International Conference on Learning Representations*, 2023.
- [35] L. Fillioux, J. Boyd, M. Vakalopoulou, P.-H. Cournède, and S. Christodoulidis, "Structured state space models for multiple instance learning in digital pathology," in *International Conference on Medical Image Computing and Computer-Assisted Intervention*. Springer, 2023, pp. 594–604.
- [36] P. Chikontwe, M. Kim, J. Jeong, H. J. Sung, H. Go, S. J. Nam, and S. H. Park, "Fr-mil: Distribution re-calibration based multiple instance learning with transformer for whole slide image classification," *IEEE Trans. Med. Imaging*, 2024.
- [37] Z. Huang, F. Bianchi, M. Yuksekgonul, T. J. Montine, and J. Zou, "A visual-language foundation model for pathology image analysis using medical twitter," *Nature medicine*, vol. 29, no. 9, pp. 2307–2316, 2023.
- [38] E. Becht, L. McInnes, J. Healy, C.-A. Dutertre, I. W. Kwok, L. G. Ng, F. Ginhoux, and E. W. Newell, "Dimensionality reduction for visualizing single-cell data using umap," *Nature biotechnology*, vol. 37, no. 1, pp. 38–44, 2019.